Lab on a Chip

RSCPublishing

FOCUS

View Article Online
View Journal

Acoustofluidics 22: Multi-wavelength resonators, applications and considerations

Cite this: DOI: 10.1039/c2lc41206c

Jeremy J. Hawkes[a] and Stefan Radel[b]

Received 31st October 2012,
Accepted 22nd November 2012

DOI: 10.1039/c2lc41206c

www.rsc.org/loc

One important niche for multi-wavelength resonators is the filtration of suspensions containing very high particle concentration. For some applications, multi-wavelength ultrasound enhanced sedimentation filters are second only to the centrifuge in efficiency but, unlike the centrifuge they are easily adapted for continuous flow. Multi-wavelength resonators are also an obvious consideration when half-wavelength chambers are too small for a specific application. Unfortunately the formula, bigger = higher-throughput, does not scale linearly. Here we describe the relationships between chamber size and throughput for acoustic, electrical, flow and thermal convection actions, allowing the user to define initial parameters for their specific applications with some confidence. We start with a review of some of the many forms of multi-wavelength particle manipulation systems.

Introduction

Musical instruments and many other resonant systems operate at their fundamental frequency, a half or a quarter wavelength. Particle manipulation chambers however, operate additionally very effectively at higher harmonics. Using multi-wavelength chambers has the advantage of more internal space, which reduces blockages while retaining higher frequencies. There are two reasons for preferring high frequencies: 1) The acoustic force on the particles increases in proportion to frequency as described in Part 7 of this tutorial series.[1] 2) Above 1 MHz, cavitation and its destructive effects, are almost absent the reasons are explained fully in Part 12 of this series[2] and therefore frequencies below 1 MHz are often avoided when working with aqueous media.

Descriptions given here will be limited to ultrasonic frequencies in the range of a few ten kHz (for aerosol-filled chambers) up to 10 MHz (for aqueous suspension-filled chambers). The devices described have internal dimensions typically in the range 1–100 mm, this size range is suitable for supporting ultrasonic standing waves (USW) in liquids and gases. This tutorial describes the use of aqueous media for most of the examples, but details are given so that designs can be created for other fluids including gases. Multi-wavelength devices are generally larger than quarter- or half-wavelength resonators, however, when very high frequencies are used, even a 50 μm channel can be a multi-wavelength device.[3]

The most successful multi-wavelength system is the Ultrasound Enhanced Sedimentation filter (also known as Ultrasonically Enhanced Settling), UES. This use of sedimentation is a different filtration principle to the filter described in parts 5, 8, 9 and 11 of this Acoustofluidic tutorial series.[4–7] In brief the latter filter (which we will identify as the hydrodynamic acoustic filter, HAF) splits lines of acoustically-concentrated cells from the clear fluid by careful flow adjustment to outlet channels, which are usually outside the standing wave region. The HAF is better suited to low cell concentrations. UES requires the formation of cell clumps and

Foreword

In the twenty-second paper of 23 in the Lab on a chip tutorial series of Acoustofluidics, Jeremy Hawkes and Stefan Radel discuss acoustic devices using multiple wavelengths. This feature can be useful for increasing the throughput of a system, and the acoustic devices are thus often constructed to be larger than most microfluidic devices. Construction of multi-wavelength resonators, as well as flow changes produced by scale-up and design approaches are discussed.

Andreas Lenshof – coordinator of the Acoustofluidics series

---

[a] *Manchester Institute of Biotechnology, The University of Manchester, 131 Princess Street, Manchester, M1 7DN, UK. E-mail: J.Hawkes@manchester.ac.uk; Fax: +44 161 306520; Tel: +44 161 3068884*

[b] *Institute of Chemical Technologies and Analytics & Institute of Applied Physics, Vienna University of Technology, Getreidemarkt 8/164 AC, A-1060 Vienna, Austria. E-mail: stefan.radel@tuwien.ac.at; Fax: +43 58801 15199; Tel: +43 58801 15142*

Table 1 Separation efficiency of plasma from whole blood comparing a centrifuge, ultrasound enhanced sedimentation (UES) and hydrodynamic acoustic filtration (HAF). UES has a clear advantage, although the final column shows a very high flow rate for a hydrodynamic acoustic filter, achieved when an additional buffer is used to overcome node overloading

	Centrifuge	UES	HAF		
	Whole blood alone				Blood + receiving buffer[8]
			1 stage[9]	4 stages	
Cells left in plasma (%)	0.01	0.3	3.5	<1	5
Recovered plasma (%)	60	40	10	10	—
Blood volume processed, ml h^{-1}	—	60	4.8	4.8	1000

so is best suited for samples with high cell numbers, such as whole blood (40% haematocrit) and for fermentation broth filtration. Its performance degrades more slowly than HAF as the nodes become overloaded. For whole blood filtration the result is clearer plasma and a greater volume of plasma produced (see Table 1). A second advantage of UES is that the dimensions are less critical even to the extent that, the UES chamber used in Table 1 and Fig. 1b and Fig. 1d was simply the Vacutainer (BD, Franklin Lakes.) used to draw the blood.

Vacutainers are an example of a batch system, however UES is often used in flow-through systems, and we will use the flow-through system as the main example for the rest of this tutorial.

With an emphasis more on construction than applications, this tutorial aims to give the reader the understanding and sources needed to design and construct a multi-wavelength chamber. We also attempt to indicate areas where new development approaches may be most valuable. The tutorial series has already covered flow dynamics (Part 1 and 10),[10,11] conditions needed for resonance (Parts 2 and 3),[12,13] devices for creating standing waves (Parts 4–6),[4,14,15] the primary and secondary acoustic standing wave forces acting on cells (Part 7)[1] and acoustic streaming (Parts 13–15).[16–18] This tutorial revisits some of these concepts to show how they have been applied to larger dimension systems and provides further details where additional considerations are needed.

The tutorial is divided into four parts so that:

Part I Acoustic filters: Gives examples of multi-wavelength resonators.

Part II Resonators: Gives an overview of the processes that have been considered in the design of multi-wavelength systems, and describes some of the observations of complex effects.

Part III Flow changes produced by scale-up: Provides tools to determine when flow becomes turbulent and also defines other limits to the flow velocity.

Part IV New design approaches: Outlines how models commonly used for Non Destructive Testing can be introduced to resonant chamber designs.

Jeremy J. Hawkes

Dr Jeremy Hawkes has been part of the miniaturisation group at Manchester University since 2002, he holds a BSc in Biophysics and received a PhD from UCNW, Bangor, Electronics Department in 1989 for a study of protein dielectric properties. He jointly founded a Dielectrophoresis Cell Characterisation lab in the Biology Department at York University before, a 9 month post doc in Nanjing, China (1993) where he first learnt how to manipulate particles with ultrasonic standing waves. This was greatly reinforced working with Professor Coakley in Cardiff, UK until 2002. Together they helped found the USWNet which continues as a community forum. His research interests now are particle manipulation in air and water with DEP and USW.

Stefan Radel

Stefan Radel received the M.S. degree in physics from the Vienna University of Technology (VUT), Austria, in 1998. He conducted his Ph.D. research within a "Training and Mobility of Researchers" program of the European Commission at University College Dublin, Ireland, the University of Wales, Cardiff, U.K., and the VUT. He received the Ph.D. degree in physics from the VUT in 2002. Since 2003, he has been with the Institute of Applied (former General) Physics, VUT. Since 2007, he is with the Institute of Chemical Technologies and Analytics at VUT. He is a member of the "Young Scientist Advisory Board" of the International Congress on Ultrasonics (ICU) and member of the committee of Ultrasonic Standing Wave Network (USWNet), as well as occasionally a scientific committee member to conferences in the regime of acoustics and ultrasound. His main research interest presently is: application of ultrasonic particle manipulation in vibrational spectroscopy.

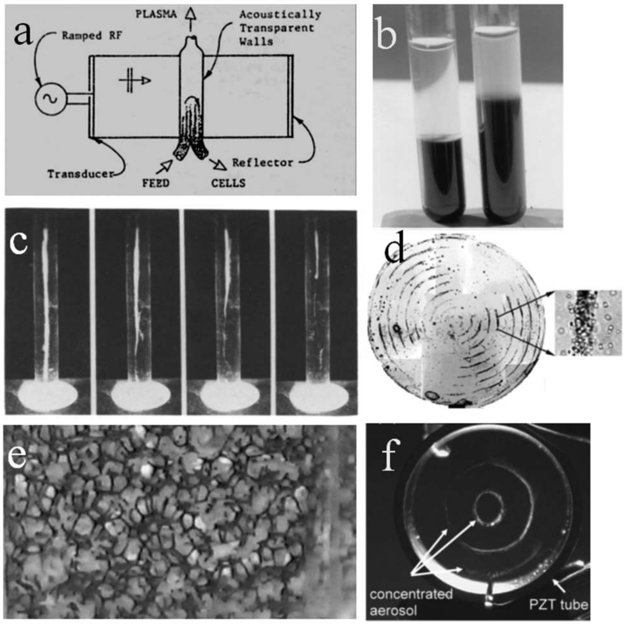

Fig. 1 Multi-wave ultrasound manipulation systems and applications in blood, water, gel mesh and air. (a) Pseudo-standing wave/sedimentation blood separator.[19] (b) Left, centrifuged blood, right, UES separation where the tube is the chamber.[20] Reproduced with permission of Elsevier Inc. (c) Pseudo-standing wave progressively lifting a column of 9 μm latex particle clumps in a 50 mm high chamber.[21] Reproduced with permission of Elsevier BV. (d) Node lines from (b) fixed in position in an agar gel, set while the sound was applied.[22] Reproduced with permission of Elsevier Inc. (e) Cells (black) adhered to a porous mesh. (f) Water droplet aerosol driven to nodes.[23] Reproduced with permission of American Institute of Physics for the Acoustical Society of America.

Part 1. Acoustic filters

This section is called acoustic filters because almost all the larger scale applications of particle manipulation are solely for filtration. Filtration is vital (and often a limiting step) for many processes. The following brief history of ultrasound manipulation chambers shows their potential to fit a very diverse range of filtration processing applications.

Peterson *et al.*[19] created one of the first clearly application-driven systems (Fig. 1a), for separating blood cells from plasma. A pseudo-standing wave was used to drive the cells across a rising flow towards an outlet which received the concentrated cell sediment. This achieved haematocrits of 80% and 1.5% on the outflows from a 40% haematocrit inflow. Cousins[20] used a fixed frequency circular wave at 1.6 MHz to enhance sedimentation directly in the Vacutainers used to draw blood, leaving only 0.3% of the cells in the plasma after <6 min (Fig. 1b). Whitworth[21] also used a pseudo-standing wave to gain impressive control of a column of 9 μm latex beads moving up and down a 5 cm high tube at up to 20 mm s^{-1} (Fig. 1c). A similar but more sophisticated node movement in harmonic steps is known as drifting field;[24] recently this transverse movement has been used to move particles out of a flow.[25] Using the Vacutainer again (Fig. 1b), the node pattern was fixed for subsequent observation by suspending cells in a viscous agar gel and allowing it to set while the sound was applied (Fig. 1d).[22] Feke[26] has used a polyester mesh, 1.25 mm pore size, to attract 99% of 30 μm diameter particles and 95% of hybridoma cells to the fibres with ∼1.12 MHz. This attraction is the result of non-uniformities in the field produced by the mesh. These effects are not limited to water or even liquids; Kaduchak (Fig. 1f)[23] and Anderson[27] have both brought aerosols of 5 μm water droplets to the nodal planes.

There are other multi-wavelength processes which do not require standing waves. The three main systems use frequencies below 40 kHz. The system most similar to the standing wave systems is for agglomeration of smoke, developed for large scale filtration.[28] In this approach the sound increases collisions between large and small particles because of their different entrainment in the oscillating air,[29] leading to increased clump formation and sedimentation. The other two multi-wavelength processes are sono-chemistry[30] and cell sonication.[31] These use the extreme pressures created by cavitation[32] to produce unusual chemical reactions and to destroy cells. These 3 systems will not be further described.

To allow more detailed descriptions the rest of the section concentrates on two systems, UES and the ''h chamber''. Both are flow-through systems with one inlet and two outlets: one for the clarified liquid and one for the enriched suspension. These systems are even more tolerant to bubbles and oversized particles than the hydrodynamic acoustic filters (themselves more tolerant than many other filters) and so multi-wave filters generally retain large channels throughout.

1.1 Ultrasonically enhanced sedimentation, UES

In brief: In ultrasonically enhanced sedimentation filters, ultrasound creates clumps as it draws single cells into vertical nodal planes. The clumps sediment against the upward moving incoming flow and highly clarified fluid emerges from the upper outlet. This approach has been developed over the past two decades mainly in commercial/industrial environments. The principle utilizes the ultrasonic agglomeration of particles bringing about a locally decreased surface to volume ratio. Due to the increased diameter of this ''super-particle'' the ratio of Stokes drag force and gravitational force lead to an increase of the terminal settling velocity of the loose aggregates and therefore higher sedimentation rates.[33–36] A quantified description is given in section 3.7.

Fig. 2 shows the stages of the UES process: in the beginning the particles are freely distributed in the liquid (a). After the ultrasonic field has built up, the axial primary radiation force drives them into nodal planes (b). Typically it does not take more than 2–3 s until such a spatial distribution is reached; at this stage bands of particles become apparent as shown in Fig. 3. It depends on the acoustic contrast between particle and liquid, if this force points towards the pressure nodes or towards the displacement nodes for a given suspension, dense particles like cells are driven into the pressure nodes.

The transverse primary radiation force further concentrates the particles within these planes (c). This force perpendicular to the sound propagation direction is less well understood but is at least partly a result of an uneven amplitude distribution over the transducer's surface. The transverse primary radiation

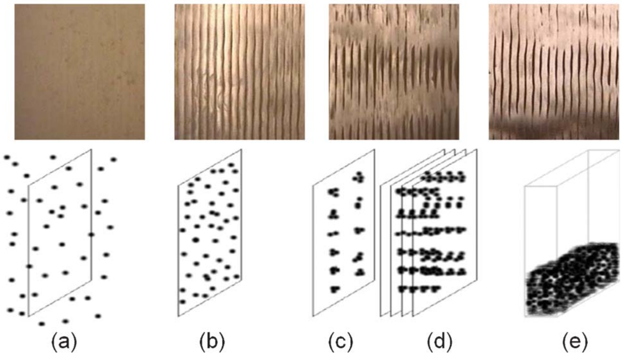

Fig. 2 Stages of Ultrasonically Enhanced Settling; homogeneously dispersed particles (a), accumulation in planes (b), and further concentrated within the planes (c), viewed as a multi-wavelength resonator aggregates are stacked in rods or horizontal columns (d). The aggregates finally settle at the bottom of the vessel (e). Adapted from ref. 37, reproduced with permission of Kluwer Academic Publishers.

force is weaker, it takes typically 10–30 s until the concentration within the planes is finished (d).

It was shown in part 10 of this tutorial series[11] that the axial force is typically greater than gravity. The transverse radiation force generally is lower and therefore these aggregates finally settle at the bottom of the vessel (e) due to gravitational force (see section 3.7).

Fig. 4 shows a pilot series UES system (USSD-05, Anton Paar GmbH, Austria); unless stated otherwise this is the design we have in mind throughout this when talking about UES. The device sits at the top of a reservoir holding the suspension. Acoustic filters are mainly used in bio-technology, hence this vessel will commonly be a bio-reactor. In applications like this the temperature of the cell suspension is of utmost importance. Therefore the liquid layer comprises two separate compartments: water circulating in the cooling layer (C) inhibits thermal stress transferred from the transducer into the adjacent active volume (AV) filled with the suspension.

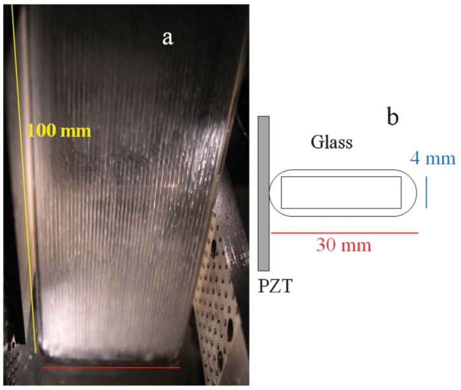

Fig. 3 a) Enhanced sedimentation of yeast, near 1 MHz, with upward flow in a vertical glass duct, viewed from above at an angle of ~30°. Showing vertical banding pattern and some accumulation at the base. b) Cross section showing piezoelectric plate, pressed on the edge of the left side, without glue.

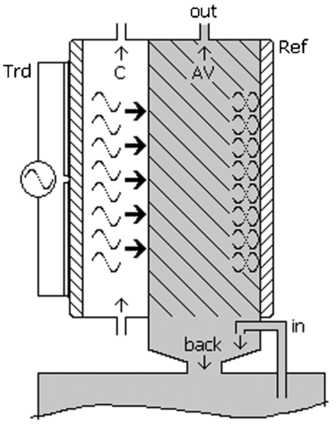

Fig. 4 UES separation on top of a reservoir, *e.g.* a bio-reactor. The ultrasound is emitted from the transducer (Trd, 25 × 25 mm^2), passing a cooling volume (*C*) and the active volume (AV) holding the suspension and finally reflected at a reflector (Ref). The thickness of *C* and AV is 12.3 and 22.25 mm, respectively. From ref. 37, reproduced with permission of Kluwer Academic Publishers.

In operation, *e.g.* as filter for perfusion reactors, the clarified liquid is harvested at the top (out). The suspension is pumped into the system from the side at the bottom (in) and together with the bottom outlet (back) this builds up a re-circulation loop by which the settled particles are immediately fed back into the bio-reactor. The vertical nodal planes allow an upward streaming of the clarified liquid between the settling aggregates.

The main advantages of cell filters based on this technique is the complete absence of moving parts and therefore absence of filter cakes or filter fouling. The systems can be hot-steam sterilized *in situ*, the materials used such as stainless steel and glass are bio-compatible. The scale-up of the technology has progressed, perfusion filtering systems capable of 200 L/d and more are commercially available, see *e.g.* Fig. 5 200 L BioSep by Applikon (Schiedam, The Netherlands).

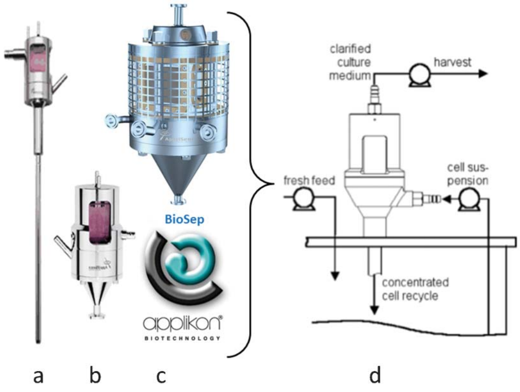

Fig. 5 Commercial Biosep filters supplied by Applikon, The Netherlands. a) 10 L d^{-1}; b) 50 L d^{-1}; c) 200 L d^{-1}. d) Sketch shows the UES on top of the bio-reactor, clarified medium is harvested at the top.

1.2 Influences on separation efficiency

The operating parameters of UES systems have been extensively characterised.[37,38] The more recent study employed a commercial UES system as described here to investigate the influence of process parameters, such as flow-through rate, cell concentration and true electric power input, on the separation efficiency for the case of yeast/saline suspensions. It was found that up to 99.6% yeast cells can be retained by the acoustic filter. Cell concentrations of 5–50 g L^{-1} wet weight and throughput of 5–20 L d^{-1}, in certain cases 46 L d^{-1}, were found to be the favourable operation conditions in a 50 L d^{-1} system. In respect to the electrical energy an upper threshold was found, at which an increase of signal amplitude, *i.e.* loudness from the acoustical point of view, did not improve the separation efficiency any further.

1.3 Splitters

In contrast to the UES principle the ordering of the ultrasonic radiation forces can also be utilized more directly in splitters. As an example of this type of ultrasonic separation systems the layout of the h-shape is shown in Fig. 6a.[39,40] The USW is exploited for separating the liquid flow lines into the cleaned outlet O1 from the particle traces into the particle enriched outlet O2.

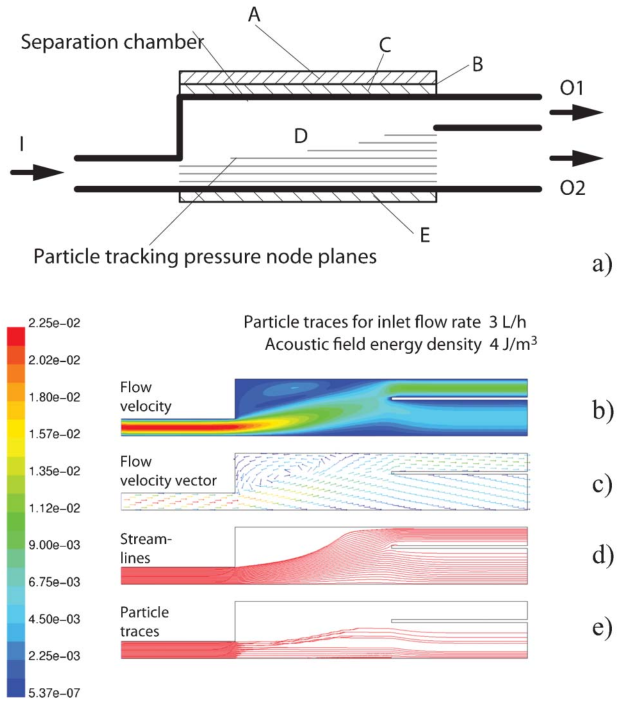

Fig. 6 Schemes of the h-shape separator. (a) On the left side the suspension is fed into inlet I of the separator, on the right side the upper outlet O1 is for the separated clean liquid and the lower outlet O2 for the particle enriched suspension. The upper wall of the active volume D (approx. 10 ml) of the system is a PZT-glass-compound-transducer (A,B,C) 50 × 19 mm^2 emitting sound towards the reflector (E) 10 mm away. (b–d) show the flow within the device when flows to outlets O1 and O2 are equal. Flow velocity (b) and flow velocity vectors (c) where determined by solving the Navier–Stokes equation for the given geometry. In (d) the velocities and vectors have been transformed to streamlines using Netwon's equations of motion. Finally (e) the radiation force is introduced, delivering the trajectories of the particles and showing their removal from the upper outlet (calculated for 20 μm polystyrene particles). Taken from ref. 41.

The concept was investigated thoroughly in a combined simulation of flow and force field, see Fig. 6b–e. The FEM simulation resulted in a maximum throughput of 3 L h^{-1} for 20 μm polystyrene particles. This direct ultrasonic separation concept is not relying on gravity. The h-separator has therefore been tested successfully under microgravity conditions in the ESA 29th zero *g* parabolic flight campaign within the frame of the ESA Melissa project.[39]

Part 2: Resonators

This section deals with various aspects, to be considered when designing multi-wavelength ultrasonic resonators (part 5 of this tutorial series[4] is more general and for sub-wavelength systems). The description assumes a simple stack of plane parallel layers as shown in Fig. 7, comprising a piezoelectric element (P) connected (glued) to a carrier layer (C) very similar to the device under test in part 9 of this tutorial series.[6] This composite transducer (T), *i.e.* the combination of piezoelectric element and carrier, emits the sound signal into a cavity holding the suspension liquid (L), which is terminated by a reflector (R) at the opposite side. In literature the liquid layer (L) is occasionally termed as active volume (AV).

2.1 Construction

A vast choice of materials for the construction of an ultrasonic resonator is available. Every application will pose its own demands, nevertheless some general remarks shall be given here along with reports about failure where it has occurred. It has to be mentioned, that the following remarks are limited to the construction of multi-wavelength ultrasonic resonators.

Regarding the piezoelectric element most applications envisaged in this work use PZT (lead-zirconate-titanate) ceramics, which are more suitable for high power applications than the well-known quartz resonators. Devices are available in different shapes and sizes and at low cost, and more importantly for almost every frequency range in the kHz to ten MHz range. A strong ultrasonic field will be excited by elements made from ''hard'' PZT types, which show high electro-mechanical coupling factors. Furthermore these mate-

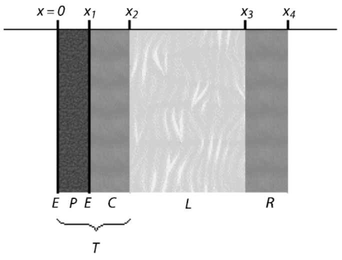

Fig. 7 Layered resonator comprising a transducer T, *i.e.* PZT ceramic P with two electrodes E glued to a glass carrier C, a liquid layer L and a reflector R. From ref. 42.

rials can be driven in resonance mode, as mechanical losses are low, a detailed discussion can be found in part 4 of this tutorial series.[14] Apart from PZT, special materials like barium titanate (lead free, low mass density) or lithium niobate (high Curie temperature) exist. In addition, new materials like single crystals from lead magnesium niobate/lead titanate (PMN-PT) or lead zirconate niobate/lead titanate (PZN-PT) are being investigated.

To employ the piezoelectric effect an electrical field is necessary, and therefore a PZT is equipped with (at least) two electrodes. Usually ''thick printed'' silver electrodes (approx. 10 μm) or thin film electrodes from gold or CuNi are available, the shape can be tailored to any needs. The excited mode is in first order governed by the geometry of the electrodes in relation to the polarisation direction; in the example used here a sheet of PZT carries electrodes at the top and the bottom. As the polarisation is oriented perpendicular to those surfaces the application of a voltage at the electrodes leads to a thickness-extension mode, and the PZT emits a plane longitudinal wave.

There are different approaches to coupling the sound from the PZT into the rest of the device, or in other words, how to build up the resonator. Some groups use a very flexible suspension of the PZT.[43] A successful method used in the past was the use of very thin layers of thermally cured glue[34] in a pressure node of the transducer (dimensions will be discussed later). Then, as the thickness of the glue layer is far below the acoustic wavelength it will be mainly displaced (''shaken'') by the USW, but not stressed. The latter would result in losses, as acoustical energy is converted into heat where a material is compressed and expanded by the excitement. One important point here is, that for high performance systems it is necessary to match the thermal expansion coefficients of the PZT and the carrier, otherwise the strong glue will lead to lateral stresses and terminal disruption of one of the two layers when in operation.

When choosing materials it is also important to remember that carrier and reflector will be in touch with the suspension, and they must therefore be adequately chemically inert. This is needed for two reasons: on one hand, *e.g.* bio-technical applications will have to be at least food-safe, but moreover might have to withstand further chemical/mechanical/temperature stresses, *e.g.* during cleaning procedures employing high temperatures, pressure and/or chemically aggressive solvents.

It is important, that materials in the acoustic pathway should show low acoustic absorption. Losses are expressed by the absorption coefficient α, when considering resonances this can be used to define the resonance quality factor

$$Q_{\mathrm{eff}} = \frac{\pi}{\lambda a_{\mathrm{eff}}} \tag{1a}$$

The expression is valid for high Q-factors ($Q \gg 1$). The Q-factor derived from the absorption coefficient α, which is governed by the viscous losses of the fluid (or any single component) only, does not describe the resonance of the whole system. For this reason the *effective* Q-factor, Q_{eff} is denoted in (1a) which represents all mechanisms attenuating the signal. Examples are losses by scattering from particles and sidewalls, and the initial loss in transduction of electrical to mechanical oscillations.

The Q-factor also serves as a measure for the ratio of energy stored, ε, by a system under investigation over the energy dissipated (see[44] and parts 2 and 3 of this tutorial series[12,13]). The latter can be expressed as time-averaged powerloss $<P^{\mathrm{loss}}>$, hence

$$Q_{\mathrm{eff}} = \frac{2\pi f \cdot \varepsilon}{\langle p^{\mathrm{loss}} \rangle} \tag{1b}$$

Hence Q_{eff} is of utmost importance for filtration describing the maximum acoustic energy stored in the liquid layer for a given electric energy supplied.

Several methods to measure the Q-factor are discussed in tutorial 6 of this series.[15,45] Intuitively the simplest (although error prone as discussed in tutorial 6) is to apply frequency bursts and measure the time, τ to rise 99.8% or ''ring-down'' to 0.2% power. The expression

$$Q_{\mathrm{eff}} = \pi f \tau \tag{1c}$$

is then used to obtain the Q-factor[15,45] for the frequency. In other words the Q-factor = π multiplied by the number of cycles in time τ.

Precision is important; an analysis of a 2 MHz resonator with a liquid layer of 32 mm[35] delivered a decrease of 10%–20% in respect to the resonance quality factor Q_{eff} when transducer and reflector were inclined by 1 mrad. Interestingly, this fall was greater for liquid layers with a higher quality factor. It was concluded, that for the system in question (L = 32 mm, transducer surface 25 × 25 mm) manufacturing tolerances should not exceed 30 μm. Therefore materials commonly found in devices are either supplied in sheet form or easily machined with necessary precision, *e.g.* metals such as brass, aluminium and stainless steel. To meet the precision requirement, flat flush-mounted gaskets as spacers/sealings are used with success. Often Perspex is found in bench top set-ups, as it is widely available and easy to machine. However, Perspex should not be used for parts within the sound path, since high absorption induces high temperatures which can potentially induce melting.

As mentioned, chemical requirements have to be met by all parts touching the suspension. In this context interestingly Borosilicate glass (Tempax, Schott, Germany) was reported early as suitable for carrier layers.[44] There are a couple of reasons for this: firstly for its chemical inertness. Also its acoustic impedance matches the needs of a transfer layer between the PZT and the suspension, which is almost always an aqueous suspension. On the down side one finds its fragility and the limited possibilities to shape glass, *e.g.* it cannot be milled. In respect to this a substitute was found in Corning Macor®, which is described as glass ceramics. It shows similar chemical and acoustical properties as glass, while being machineable, and thus allowing for more complex shapes of transducer carrier layers. Glass is also used as reflector adding the possibility for visual inspection often needed for reasons of control. The identification of glass as a suitable material led to the use of glass cuvettes in the industrially available acoustic filters.[46]

2.2 Tools for development

There are principal challenges connected with the design and evaluation of ultrasonic resonators. One is, that sound fields spread throughout a device - especially if a set-up comprises materials with low acoustic attenuation – and often one ends up with a multimode vibration state much more complicated than foreseen. The number of modes increases with dimension, simply because more harmonics can be excited. This tendency is therefore intensified in multi-wavelength devices.

Another challenge is that USWs and the resulting radiation forces are hard to measure *in situ*, because any sensing device, for instance a hydrophone, will alter the field by its mere presence. A method for high-precision observation of the particle movement to evaluate the acoustic pressures and radiation forces has been presented in[47,48] and part 7 of this tutorial series.[1] In multi-wavelength devices, however, the view onto the particles is often obstructed, hence another helpful method to freeze the spatial distribution, *i.e.* the effect of the forces for further examination has been developed[22] (see section 2.4).

2.3 Models and measurements

When designing a resonator for a defined purpose it is valuable to evaluate different approaches prior to construction of a set-up as the latter step is time consuming and expensive. Very helpful at this stage is a model, *i.e.* a mathematical description of the sound field to be expected based on the properties of the various parts of the set-up (dimension, shape, materials). Moreover a model is also useful to test a given proposition for having the desired characteristics and, to a certain degree opens the possibility for improvements during construction. It is of low significance, if an analytical model[49–51] or a numerical method like FEM[14] is applied, as long as the geometrical configuration can be described properly.

A second pre-requisite is a measurement device. Electrical measurements are commonly made over a frequency range at the PZT electrodes. Depending on the measurement apparatus applied (simple oscillator, impedance analyser, phase locked loop, *etc.*) the absolute or complex values for impedance/admittance over frequency become available. For the latter case measurements with dedicated systems designed in-house[52,53] or network analysers[54] have been carried out. Recently a commercial device (Z-Check, SinePhase) for this purpose has become available.

When performing high-precision measurements, one has to be aware that the device under test seen by the measurement and driving electronics comprises the piezoelectric element and an additional static capacitance C_0 caused by connectors and cable, but foremost by the device's electrodes. These are facing each other and therefore represent a simple electric capacity. The well-known Butterworth-van-Dyke equivalent circuit for piezoelectric elements models these influences as parallel capacity, when evaluating the measurements this capacitance has to be compensated for.[35,55]

As mentioned, the process of evaluating a resonator in question is iterative. The natural starting point is the PZT itself. Here often the material properties are available from the manufacturer, hence the properties of the explicit specimen can be tested by a measurement/simulation comparison. To be more precise, usually mass density and speed of sound values in data-sheets are of high quality, however electromechanical coupling factors given tend towards the theoretical maximum. Thus using a measurement, the best specimen out of a group can be chosen.

The next step is the fabrication of the composite transducer, *i.e.* the glueing process. Now already some material parameters of the carrier (and the glue, if taken into account) might be missing, and can be estimated iteratively. If possible, it is of some use to compare measurements of the isolated transducer, (*e.g.* lying on cotton wool) with measurements when the transducer is connected to the empty resonator cavity. Strong differences in such measurement results indicate an excitement of the device itself, possibly interfering with the main target to carry acoustic energy into the suspension.

The final step is the evaluation of the resonator filled with a well-characterised liquid, *e.g.* distilled, degassed water or alternatively with the pure host liquid used in the desired application. A resonator characterised in this way can be very valuable, when dealing with suspensions of unknown properties (as will be the most common scenario). As only the parameters regarding the sonicated volume are influencing the measurement, just a handful of parameters are to be fitted.

Simulation-supported measurements were used to estimate the dependency of the acoustic quality factor on the particle load.[42] A simple cuvette resonator was filled with suspensions of yeast cells at various concentrations. Measurements of the admittance were fitted with an analytical model,[50] the presence of 5 g L^{-1} bakery yeast did lower the original quality factor of 6000 moderately to 5300, an addition of 50 g L^{-1} however led to a considerably decreased value of 3000. The comparison delivered a relation of

$$Q_{\mathrm{susp}} = Q^{\mathrm{l}}_{\mathrm{eff}} e^{-0.1 c_{\mathrm{Y}}} \tag{2}$$

between the resonance quality factor Q_{susp} of the resonator filled with suspension at a cell concentration c_{y} and the value for $Q^{\mathrm{l}}_{\mathrm{eff}}$ when the liquid layer consisted of pure host liquid, in this case water. The coefficient in the exponent is specific for the respective resonator, for a different device a value of 0.08 was found.

One successful application of this process of comparing measurements and modelled data was the assessment of the driving frequencies of a multi-wavelength resonator. Typically these devices show spectra as in Fig. 8a. The admittance over frequency is dominated by the transducer resonance, *i.e.* the main trend in Fig. 8a, which is superimposed by a large number of ''water resonances'' (see as well part 4 of this tutorial series[14]).

Two characteristic frequencies are marked in Fig. 8a: f_1 coinciding with the fundamental resonance frequency of the piezo ceramic and therefore electrically most strongly pro-

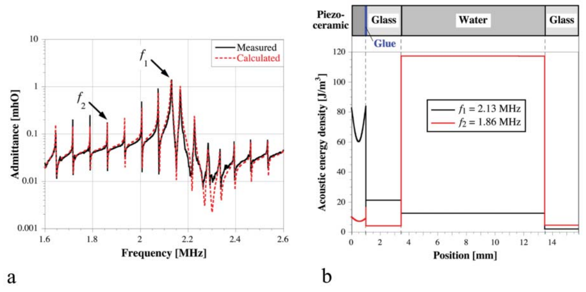

Fig. 8 Investigation of two resonance frequencies. (a) Electrical admittance, (b) spatial distribution of energy density at 4 W_{rms}. Taken from ref. 41.

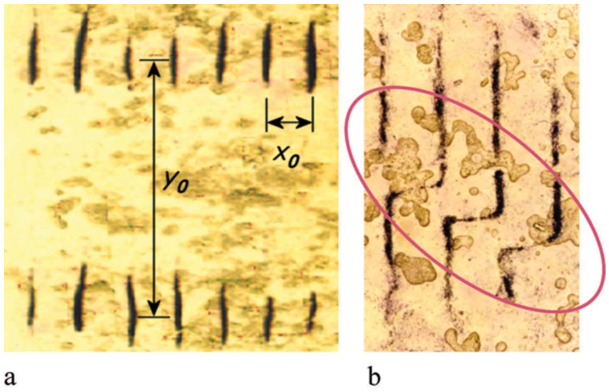

Fig. 9 Light micrographs of a gel-block cut parallel to direction of sound propagation (a) Representation of the influence of the primary radiation forces. The half-wavelength was measured to be x_0 = 379.6 ± s.d. 21.7 μm, the distance between the columns was y_0 = 3427.7 ± s.d. 88.9 μm. (b) The ''dancing of the cells'', *i.e.* cells streaming from one pressure nodal plane to another (see red mark) is not explained theoretically yet. Adapted from ref. 56, reproduced with permission of Kluwer Academic Publishers.

nounced, and f_2, which seems to be less optimal due to its lower admittance.

Fig. 8b shows the acoustic energy density along the axial direction of the resonator calculated by an analytical model.[50] The graphs represent the results for the two selected frequencies f_1 (black) and f_2 (red). Surprisingly, the maximum energy density in the suspension layer was found at the electrically much less pronounced system's resonance f_2. Thus, the optimum system performance is achieved at resonance frequencies not coinciding with Eigenfrequencies of the piezoelectric ceramic. For practical reasons even the opposite is true: at f_1, one would face heating of the transducer due to the high energy density in the piezoelectric element.

2.4 Gel technique

For the investigation of the sound-generated spatial arrangement of particles within a multi-wavelength device, a novel technique was developed overcoming the reconfiguration of ultrasonic fields upon any change of environment, *e.g.* the use of a hydrophone. The liquid fraction of the suspension was replaced by a gel initiated polymerization chemically or thermally entrapping the particle arrangement during the application of the ultrasonic field. Thus the particles were ''frozen'' at their positions caused by the ultrasonic forces. The resulting gel-block could be retrieved for further examination with a range of microscopy methods.[22,56]

In Fig. 9, a set gel formed from a yeast/polyacrylamide suspension was sliced and examined by light microscopy. With this method it was possible to evaluate the influence of the axial and transverse primary radiation force separately. The periodical variation of the axial primary radiation force in direction of sound propagation was reflected by the cells' organization in lines corresponding to the USW's pressure nodal planes (see Fig. 9a).

An aberration of the predicted behavior was detected (see Fig. 9b) where cells were concentrated in regions along the direction of sound propagation. This phenomenon is dynamic, *i.e.* the cells stream from one nodal plane to the next one in direction of sound propagation.

The gel-method allows for more sophisticated assessments; Fig. 10 shows the results of a laser confocal microscopy investigation of the ultrasound field within a cylindrical resonator used for increasing the sensitivity of agglutination tests for clinically relevant compounds such as meningitis-causing bacteria.[57] The results reveal a structure of three cylindrical shells in which particles are concentrated.

Of interest for the construction of microfluidic applications might be the possibility to apply electron microscopy assessments to a gel specimen. Fig. 11 shows a scanning electron microscopy image of the inner structure of an aggregate of yeast cells. The picture suggests, that the cells are not touching each other and therefore the supply with nutrients and oxygen can be assumed for cells within an USW.

From the experiments in these studies, an additional important observation was made, when yeast cells were concentrated in the nodal plane in a nutrient gel (data not shown). After a four day incubation the amount of biomass at the location of the agglomerate significantly increased, indicating that the yeast cells were able to reproduce.[22] Thus the exposure to an USW did not harm yeast cells. It has

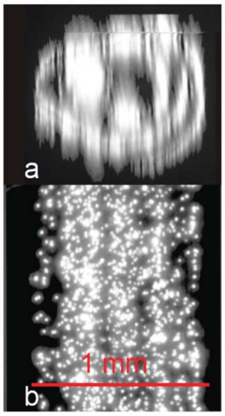

Fig. 10 Confocal microscopy of the gel rod retrieved from a cylindrical resonator driven at 3 MHz. Radial (a) and axial (b) sections of fluorescent particles in a rod of alginate gel. The particles are concentrated along three surfaces of vanishing pressure.[22] Reproduced with permission of Elsevier Inc.

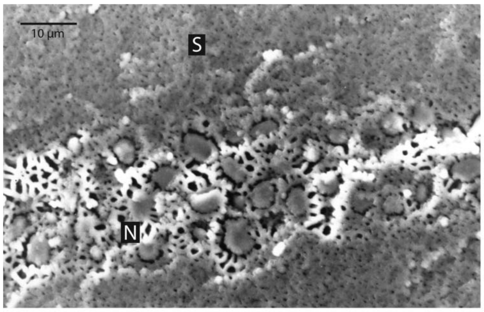

Fig. 11 SEM image of a single band as shown in Fig. 9. It shows the yeast cell distribution within the band and the structure of the treated gel. A rare net (N) of gel formation is visible within the band around the single cells. A more compact structure (S) is formed in the inter-nodal space. The fracture was performed along the band. From,[56] reproduced with permission of Kluwer Academic Publishers

previously been shown that megahertz sonication does not significantly affect yeast cell viability.[58] Only when the cells left the pressure nodes of the USW were significant alterations of viability and other similar parameters observed.[37] Detailed information about cell viability in microfluidic acoustic resonators can also be found in part 12 of this tutorial series.[2]

The use of the gel-technique was further employed to confirm a report[59] about the change of resonance frequency in multi-wavelength devices while the familiar arrangement of particles was brought about by the USW. Measurements of the true electrical power input *vs.* the frequency of a layered resonator (shown in Fig. 7) were conducted (data not shown) with the ''suspension'' layer consisting of a gel-block with suspended yeast.[42] Data from randomly distributed cells was compared to data acquired when an USW was used to arrange the cells prior to gelation. The result was a significant influence on the resonance frequency by the ordering of cells in the pressure nodal planes, the re-arrangement by the USW influences the properties of the resonator as a whole.

2.5 Control of acoustic signal

It is necessary to be able to control the driving frequency for a stable operation for several reasons: One is the mentioned change in frequency as cells come into the nodal planes and agglomerate, hence it is necessary to tune the signal when this happens. Moreover, the speed of sound is affected by the temperature[60] and so is the wavelength. Consequently resonance conditions are not met when the system's temperature changes, i.e due to dissipation. Correct tuning of the driving frequency was accomplished by controlling and/or logging the temperature change[8,48] or measuring the excitement.[33,61]

Additionally of course electronic measurements are available. In this context it is important the chosen electrical criterion meets the acoustic behaviour. It was shown,[35] that for resonances between the transducer Eigenfrequencies *e.g.* f_2 in Fig. 8a, high acoustic energy density in the liquid layer coincides with the maxima of the true power consumption, which could easily be utilized by the control electronics to tune the system properly. This resulted in high performance numbers,[44] *i.e.* optimal usage of a given electrical power consumption.

2.6 Dimensions

Transducer (T). The composite transducer (T) consists of the PZT covered with electrodes on either side and this layer glued to each other (see Fig. 7). Experience shows, that for frequencies in proximity of the piezoelectric elements resonance frequency, the glue layer can be neglected. For frequencies away from the PZT Eigenfrequency however some influence can occur.[54]

The reason is that around the PZT's resonance, *i.e.* when an odd multiple of half wavelengths (usually one) fit into the piezo layer the glue layer is situated in or close to a pressure node, hence no forces are exerted. An analysis showed that some applications benefit from carrier plates close to odd multiples of a quarter wavelength. This however means, that stress on the glue layer will not vanish and the type of glue is of importance; thin layers of low-viscosity types were used successfully.

Reflector (R). The perfect reflector, *i.e.* showing a reflection coefficient of 100% would be the termination of the resonator by a liquid-vacuum interface. However, such a ''free end'', *i.e.* a pressure-free boundary condition is obviously not practical. For construction purposes the termination by a layer showing a high acoustic impedance (hard and heavy) has turned out to be the best solution. To minimize the power loss in the reflector, the material should have low mechanical absorption; the thickness should be a (small) odd multiple of a quarter of the wavelength. This dimension leads to a standing wave with small amplitude (destructive interference) within the reflector expressing a pressure antinode at the interface with the liquid layer.[6,62]

For certain applications the use of microscopy cover slips or other thin reflectors was reported.[33,63] These are thinner than ¼ wavelength yet they are very efficient reflectors, probably by producing a condition similar to a liquid terminated by a vacuum.

2.7 Thickness limits and scale considerations

Multi-wavelength resonators usually work well with acoustic path lengths up to a few tens of millimetres. They are often used with high particle concentrations, hence attenuation poses a limit. A strong resonance occurs when a wave is reflected many times along the same path. Attenuation by the suspension will lead to the situation in Fig. 12: Due to the damping the amplitude of the standing wave depicted by the grey envelope is strongest at the reflector and decreases across the cavity towards the transducer. This decrease is dependant on the thickness of the liquid layer. When attenuation reaches a point where only one significant reflection is expressed, the filtration breaks down because the amplitude of the returning wave becomes too low and particles are not held in place by the radiation forces. In addition, a residual propagating wave always exists (red line in Fig. 12), as the reflected wave's amplitude interfering with the incoming wave (and thus building up the standing wave) has decreased. This travelling share will induce turbulent streaming, and particles will be

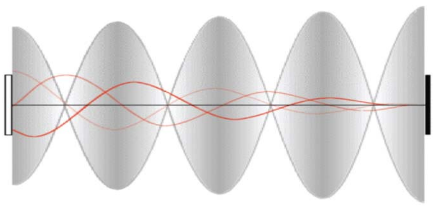

Fig. 12 A standing wave (indicated by the amplitude envelope fixed in space) and a residual propagating wave (depicted by the red lines showing the displacement at different times). Adapted from ref. 42.

dragged from the transducer towards the reflector. The phenomenon is known as Eckart streaming.

The preceding description about dimensioning is rather straight forward, the reader is referred to ref. 64 if interested in high performance applications from the industrial point of view, *i.e.* consideration of efficient use of electrical power, precise prediction in respect to heat production *etc.*

2.8 Acoustic contrast

The observation of a steady movement of particles and liquid from the transducer towards the reflector can also be due to the lack of acoustic contrast between particles and liquid. The acoustic contrast in a standing wave is well known as a coefficient in the calculation of the axial primary radiation force determining whether this force points towards the pressure or the displacement nodes for a given suspension. For a travelling wave the acoustic contrast can only be positive, the respective force always points in direction of wave propagation.[65]

Fig. 13 shows the ratio of the acoustic contrasts in the plane of mass density ratio Λ and speed of sound ratio σ of particle and liquid. In other words, the material properties of a given suspension correspond to one data point in Fig. 13. The important fact is that acoustic contrasts for propagating and standing wave reach zero for different combinations of Λ and σ. That means, that for suspensions with certain characteristics – in the black region in Fig. 13 – the force of the standing wave becomes very low or zero while the force of the propagating wave – although usually being much smaller – is still exerted on the particles. As a residual propagating wave is always present (see Fig. 12), particles are driven through the resonator.

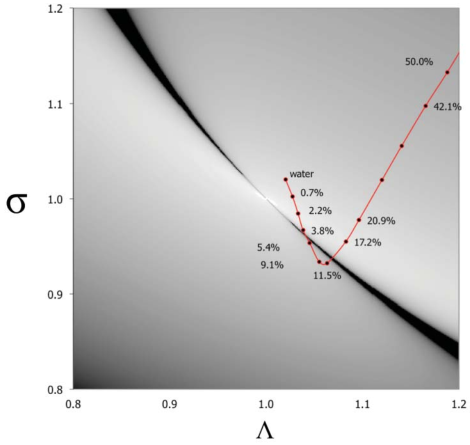

Fig. 13 The acoustic contrast factor ratio K_p/K_s of a progressive and a standing wave over mass density ratio Λ and soundspeed ratio σ of particle and liquid. Dark regions depict high values where K_p is exceeding K_s . As both coefficients are zero for different values the ratio reaches infinity (within the black regions). The red line refers to specific values of yeast cells suspended in water-ethanol mixtures, numbers give the ethanol concentration. Taken from ref. 42.

For yeast cells in water-ethanol mixtures – the red line in Fig. 13 indicates material properties of mixtures with increasing ethanol concentration – this was observed to cause decreased viability and changes in the morphology.[37] It should be emphasized that the standing wave was present; however due to the lack of acoustic contrast the respective radiation force was not exerted on the particles.[42]

Part 3. Flow changes produced by scale-up

3.1 Non-turbulent flow required

Well organised movement of particles into nodal locations is severely disturbed by flow crossing between nodal planes but not by flow along the planes. Turbulence is usually the only source of flow across nodal planes. In sections 3.2 to 3.6 we give some practical examples for predicting the onset of turbulence so that it can be virtually eliminated at the system design stage. In section 3.7 the maximum flow rates for a non-turbulent UES system are defined.

In channels less than 1 mm across turbulence is difficult to produce but, as the dimensions increase turbulence becomes progressively more probable. In multi-wavelength systems the dimensions are usually large and so considerable care must be taken to avoid turbulence. However once turbulence has been eliminated from a system the flow will be laminar, and in this condition most of the flow properties can be calculated very accurately. Part 1 of this tutorial series[10] and other texts[66] describe the concepts required for calculating many properties in the laminar flow regime. Here we will give one example, simplified to 2 dimensions: In straight channels the flow is parabolic (as seen in Fig. 14, width w = 8 mm); the velocity v_z of each band at distance z from the centre of the channel is described by:[67]

$$v_z = \frac{6Q'}{w^3}\cdot\left(\frac{w^2}{4}-z^2\right) \qquad (3)$$

where Q' is the flow rate through a channel of unit depth (note we are using ($'$) to distinguish flow rate Q' from the resonance Q-factor).

The certainty of velocity at each position in a laminar flow, together with the certainty of acoustic node positions in principle allows complex hydrodynamic manipulation downstream from the sound field as described for sub-wavelength systems in parts 2, 5, 7, 8, 9,10, 11 of this tutorial series.[1,4–7,11,13] However, surprisingly there are as yet no examples where hydrodynamic manipulation is used in combination with systems of more than two wavelengths.

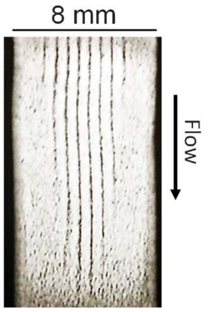

Fig. 14 Parabolic flow profile $Q' = 0.1$ ml s^{-1} visualised by, bands of yeast cells a few seconds after switching on 9.9 MHz sound in a 10 mm deep × 1.1 mm wide resonating channel, which has been expanded to 8 mm wide downstream from the sound field, without disruption to the parabolic flow. Adapted from ref. 68. Reproduced with permission of Elsevier BV.

3.2 Calculating the onset of turbulence

There are no high-precision methods to calculate the exact condition where laminar flow will become turbulent, and so to prevent turbulence our designs should allow a large margin for error and err on the side of caution. The Reynolds number is a good indicator of turbulence, the probability of flow changing from laminar to turbulent increases rapidly when the Reynolds number is large, usually between 500 and 2000.[69] The lower value is used in examples here, since any flow detachment from the walls and not just full vortex shedding can reduce particle manipulation efficiency.

The design process for a new system should start with the analytical calculations set out below. If this leaves any uncertainty about the possibility of turbulence then, although many more equations are available, the next step is usually to carry out initial tests either using 3-dimensional models or physical experiments.

3.2.1 Reynolds number dependence on duct profiles. For an infinite length parallel sided tube the Reynolds number is given by:

$$\mathrm{Re} = \frac{\rho_f v_{av} L_0}{\eta} \tag{4}$$

where ρ_f is the fluid density, v_{av} is the average velocity through the tube obtained from cross section area/flow rate Q', and η is the dynamic viscosity of the fluid.

L_0 the length scale[10] also known as D_h hydraulic diameter is the tube diameter for circular cross section tubes. When considering non-circular ducts of area A, the length scale is obtained from:[70]

$$L_0 = \frac{4A}{\text{wetted perimeter}} \tag{5a}$$

For rectangular ducts this is

$$L_0 = \frac{4wd}{2(w+d)} = \frac{2wd}{(w+d)} \tag{5b}$$

where w is the width and d is the depth of the channel.

3.3 Effect of scale up on the initiation of turbulence

Here we define the relationship between scale up and the switch to turbulent flow, for long parallel-sided ducts, such as the main channel of the UES filter.[36,71]

The upper flow rate Q'_{max} for laminar conditions (we are defining this condition as Re = 500) is obtained from eqn (4) and (5b) as:

$$Q'_{max} = \frac{500\eta A}{\rho_f L_0} \tag{6}$$

In water filled square ducts:
1 × 1 mm, $Q'_{max} = 0.45$ ml s^{-1}, $v_{av} = 450$ mm s^{-1}.
10 × 10 mm, $Q'_{max} = 4.5$ ml s^{-1}, $v_{av} = 45$ mm s^{-1}.

This small advantage gained by increased channel cross section is shown as the lower (blue) line in Fig. 15. Two better solutions for scale up are also shown in Fig. 15; these are:

1) Increase only one dimension.
2) Use many parallel channels.

The compromises from these two low dimension, high velocity scale-up solutions are: increased blockage potential from oversized particles and, an increase in inter-channel wall area and a need to supply equalised ultrasound levels to all channels.

For enhanced sedimentation systems slightly larger chambers are possible since the maximum sedimentation velocity at 1 MHz is 10 mm s^{-1} (calculated in section 3.7), whereas the observed upper velocity in hydrodynamic separation systems is ~50 mm s^{-1} (5 μm diameter particles in a 10 mm field length[67]). At these flow velocities, in square ducts, flow becomes turbulent at 45 and 9 mm widths respectively.

3.4 Heating

Convection from heating introduces a further mechanism for fluid movement which may destroy particle alignment. In vertical chambers, when one wall is at a higher temperature than the opposite wall (*e.g.* heated by the presence of an ultrasound transducer[5,74]), fluid against the heated wall rises and falls near the opposing wall, forming a chamber-high circulation as shown in Fig. 16a.[72,73] However, one circulation is not a significant problem when the nodal planes are vertical

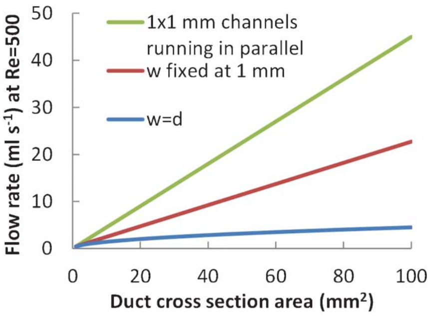

Fig. 15 Maximum non-turbulent flow rates for three parallel-sided channel geometries, square, aspect ratio increased with area and multiple square 1 mm^2 channels. Calculated for water filled ducts $\rho_f = 997$ kg m^{-3}, $\eta = 9 \times 10^{-4}$ kg m^{-1} s^{-1}, $g = 9.8$ ms^2. Flow rates at the onset of turbulence (identified as Re = 500).

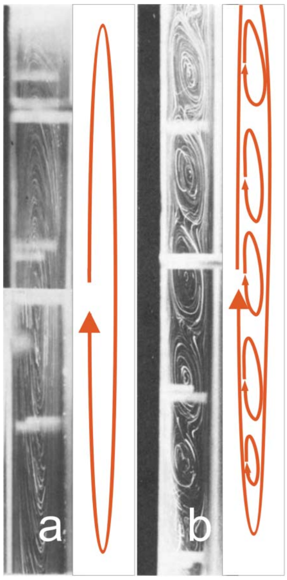

Fig. 16 Flow lines in a vertical duct heated on the left wall to a constant temperature. The streak photographs show 0.2 mm polystyrene spheres (acting as flow tracers) moving through transformer oil. $h/w = 15$ ($w = 20$ mm). a) Whole channel circulation Nu = 53. b) Circulation breaks into multiple vortices Nu = 65. Photographs[72,73] reproduced with permission of Cambridge University Press.

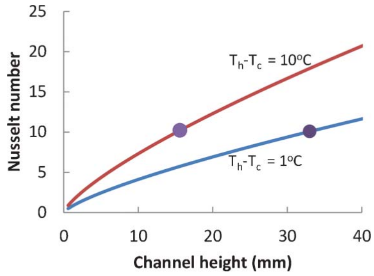

Fig. 17 Dependence of thermal convection, indicated by the Nusselt number, on chamber height with 1 and 10 °C gradients across a parallel plate chamber. Disruptive convection (multiple vortices), in water, occurs with Nusselt numbers above 10 in water. The markers show Nu = 10 at 1 °C and 10 °C temperature gradients indicating the maximum acoustic chamber heights for these temperature gradients. Calculated for water filled channels with aspect ratios $h/w = 3$. $\alpha v = 0.256 \times 10^{-3}$ kg m^{-1}s^{-1}, Cp = 4180 J kg^{-1} °C^{-1}, $k = 0.607$ W m^{-1} °C^{-1}, $g = 9.8$ ms^{2}.

since it causes little cross over between nodal planes in the central region of the chamber. Further heating increases the circulation velocity and a new regime occurs where the flow takes short cuts to the opposite wall forming smaller vortices, and this is disruptive for vertical alignment of particles. In water the new flow pattern may be much more complex than the stable pattern shown in Fig. 16b. There is no precise definition for when the disruptive circulation will begin but convection becomes significant when the Nusselt number Nu (Convective heat transfer/conductive heat transfer) is above 1, and in water disruptive vortices have been observed for values above 10.[75]

A calculation of the Nusselt number depends on conditions, in the stable conditions which we are interested in then for a chamber height h and width w the Nusselt number is given empirically as,[72]

$$\mathrm{Nu} = 0.36\mathrm{Pr}^{0.051}(h/w)^{-0.11}\ \mathrm{Ra_h}^{0.25} \tag{7}$$

Where, Pr (Prandtl number) = υ/κ, υ = kinematic viscosity (η/ρ_f) and κ is the thermal diffusivity $k/\rho\mathrm{Cp}$, where k is the thermal conductivity of the fluid and Cp is the specific heat capacity.

$\mathrm{Ra_h}$ (Rayleigh number for the chamber height) = Gr Pr where Gr (Grashof number) = $g\alpha_v(T_h - T_c)h^3/\upsilon^2$. g is acceleration due to gravity, α_v is volumetric thermal expansion coefficient, T_h and T_c temperatures of the hot and cold walls.

Fig. 17 shows Nusselt numbers for chambers of differing heights where $h/w = 3$. The figure shows that Nusselt numbers near 10 are obtained from 1 °C heating in a 33 mm high chamber or 10 °C heating in a 15 mm high chamber. Since the chamber width has little effect on the Nusselt number a general rule is that the chamber height should not greatly exceed 30 mm and if high temperature gradients cannot be avoided smaller chambers should be used.

In 1 mm high chambers up to nearly 20 mm wide, the Nusselt number remains below 2 with a 10 °C temperature gradient. For chambers heated from below the Rayleigh number can be used to determine the onset of convection, the critical value in this case is 1700.[73] In a 1 mm high chamber this is reached with a 90 °C temperature gradient while in a 50 mm high chamber (See Fig. 1c) convection will start with a 7×10^{-4} °C temperature difference. When convection starts in chambers where h/w is small, it breaks into small Rayleigh–Bénhard convection cells, and when particles are present the cells organise the particles into patterns which could easily be confused with acoustic particle clump formations.

We can conclude that for chambers where $h < 1$ mm thermal convection is unlikely. In tall systems with horizontal acoustic nodes, convection crossing the nodes will cause some disruption as shown by two observations in a 50 mm high × 10 mm diameter tube (extensively used for observing horizontal nodes, where sedimentation is absent): On the lab bench without heat sources convective flow was typically 100 µm s^{-1}, a temperature increase of 2 °C was observed after applying sound for 1 min and this increased the convection to 200 µm s^{-1}.[76] 1.3 µm diameter particles could not be held in 1 MHz nodal planes with this level of flow across the nodes. However in a microgravity experiment convection stopped within 1 s and the particles were brought to the nodal planes until collapsing when gravity returned.[77]

3.5 Entrance condition

When a turbulent fluid enters a channel with a Reynolds number low enough for laminar flow to develop, it travels some distance before all turbulence ceases and a fully developed parabolic flow profile forms. The maximum entrance length L_e for fully developed laminar flow has been refined by a number of authors.[78–81] A straightforward approximation for Reynolds numbers in the region of 100 was given in part 10 of this tutorial series.[11]

$$L_e = \frac{l_0 \mathrm{Re}}{24} \tag{8}$$

For square section ducts with a flow rate at Re = 500 the increase in entrance length with width is shown in Fig. 18. In a 1 × 1 mm duct L_e is long at 21 mm, in a 10 × 10 mm duct it extends to 210 mm. Since large systems are usually operated at higher Reynolds numbers the entrance length becomes increasingly important but curved parts as described in the next section can be used to reduce the length.

In systems with adjacent flow,[82] which is a technique used extensively in sub-wavelength system[83] and described in this tutorial series Part 8,[5] a failure to observe the entrance length criteria can twist the flow so that side by side flows become above and below, only in extreme cases would detached vortices be seen.

At constant flow rate, the entrance length falls with increasing fluid viscosity.[22]

3.6 Flow expansion and contraction without disruption or dead volumes

When flow in a channel is laminar, expanding the channel can give three possible outcomes, dependent on the angle of expansion, as shown in Fig. 19: (A) Full turbulence with vortices shedding from the discontinuity, these can be detrimental further downstream in the system. (B) Attached vortices, and flow line separation from the wall (see Fig. 6B top left corner for example), when this happens the streamlines become concentrated at the centre (the pressure drop at expansion can actually become a pressure increase as the flow become squeezed to the centre lines). Alternatively if streamlines follow the expansion with no separation from the wall then no turbulence develops (C and D).

The detachment criteria have been identified for aerofoils[84] but not for liquids, where precision is needed. Chemical engineering texts[70] recommend numerical modelling. However some early experimental work with channels (∼40–100 mm wide) provide good indicative values which are similar to computational fluid dynamic model values:[85] In large water-filled ducts no flow separation (C) was observed when the angles between the diverging walls of circular channels was <5°, and 11° for one-dimensional expansion in rectangular ducts[86] (14° for air[87]). In contracting ducts detachment is less likely and not usually seen with angles <45°. The flow patterns A–D appear to be almost independent of flow rate[86] and scale for example, flow streaming (similar to B) is known to occur around spheres down to the scale of cells.[16,17] Scale independence allows very large expansions, such as upstream from Fig. 14 where the channel expanded 7-fold (1.1 mm–8 mm) at up to 20° without measurable disruption to the particle formations created with ultrasound.[67] This steep angle is probably partly achieved by the use of curved walls designed to follow the flow lines as shown in (D).

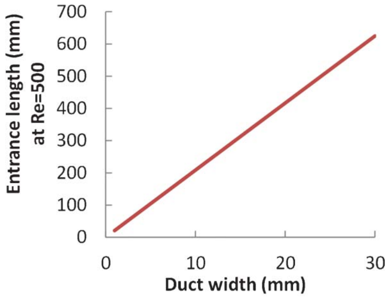

Fig. 18 Relationship between the entrance length L_e required for fully developed laminar flow and the duct width. Calculated for square cross-section ducts Re = 500 *i.e.* the flow rates vary but remain just below the transition to full turbulence.

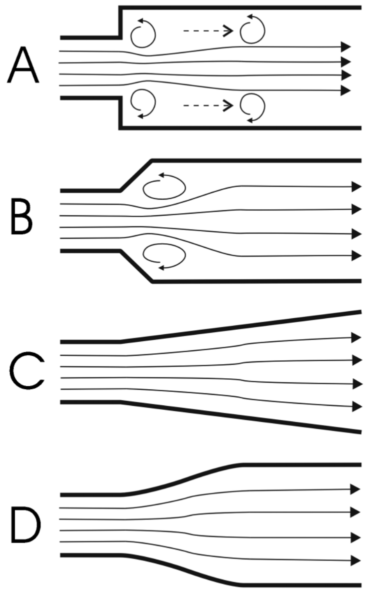

Fig. 19 Channel expansion. A) At high flow rates an abrupt expansion produces vortex shedding. B) Less abrupt expansion produces stable attached vortices and separation of streamlines from the walls. C) Low angle expansion maintains fully formed laminar flow. D) Curves decrease the length required for expansion.

In some systems separation from the wall may be unavoidable, this creates dead-volumes, however provided the vortices remain stable their presence may be acceptable. Instability of the vortices leads to fluid oscillations throughout the system and should be avoided. Detachment *i.e.* full turbulence (A) (indicated by pressure drop) should of course always be avoided, it occurs with expansion angles >60°.

3.7 Enhanced sedimentation

A general calculation of sedimentation from part 10 of this tutorial series,[11] can be used to calculate the filtration efficiency of the UES filter (described in section 1.1). Good agreement with experiments is obtained by assuming that the clumps are spherical and reach diameters of one quarter of a wavelength[36] (at 1 MHz: each clump contains 50,000 5 μm diameter cells). The gravitational force acting on cell clumps of radius r_c, density ρ_c, is given by:

$$F_g = \left(\frac{4}{3}\right)\pi r_c^3(\rho_c - \rho_f)g \tag{9}$$

Viscous (Stoke's) drag on the clump moving at velocity v_c in a fluid moving at velocity v_f is given by $6\pi\eta r_c(v_f - v_c)$. At its terminal velocity v_c the gravitational force is fully opposed by the viscous drag force and when the sedimentation velocity is equal to the rising fluid velocity then $v_c = 0$ and:

$$6\pi\eta r_c(v_f - v_c) - \left(\frac{4}{3}\right)\pi r_c^3(\rho_c - \rho_f)g = 0 \tag{10}$$

We find:

$$v_f = \frac{2r_c^2(\rho_c - \rho_f)g}{9\eta} \tag{11}$$

This upper limit for sedimentation against a rising flow is shown by the red line in Fig. 20. Since the maximum clump diameter is ~ ¼ wavelength, $\lambda/8$ can be substituted for r_c to find the frequency-dependent maximum velocity of clarified fluid through the system, plotted as two data points in Fig. 20.

The calculation of maximum velocity assumes that the ultrasound field is long enough for most particles to arrive at the nodal plane[11] and also that the input concentration is sufficient to form large clumps.

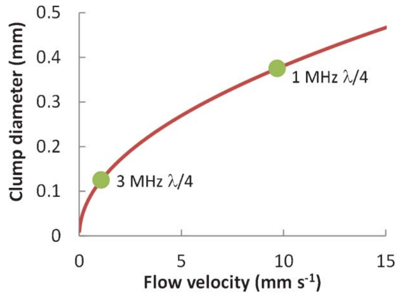

Fig. 20 Diameters at which cell clumps no longer sediments against an upward flow. Markers show clumps with diameters equal to a quarter wavelength at 1 MHz and 3 MHz which, indicate the maximum flow velocities for filters operating at these frequencies. Calculated for an aqueous suspension of yeast ρ_c 1.114 × 10^3 kg m^{-3} . Adapted from ref. 36.

Part 4. New design approaches

4.1 Heating mitigation

At low power, mechanical losses in the transducer and at interfaces are the main source of heat, while at high power levels electrical losses in the transducer overtake mechanical losses and the piezoelectric ceramics can become very hot (sufficient to depole the transducer *i.e.* ~200 °C).[88] Mechanical losses are often controllable and it is possible to run transducers at 5–10 °C above ambient, although of course temperature differentials make particle manipulation increasingly unstable (due to loss of resonance and convection). Best results are usually obtained with no part heating by more than 1 °C. When maximum power is needed, outputs have been pushed upwards 2–3 fold by adding some form of cooling; in sub-wavelength devices the piezoelectric element has been separated from the chamber wall with a metal block heat sink cooled with a Peltier element.[8,48] Separation is also used in larger devices where forced water cooling replaces the metal block;[33,71] or an alternative is forced air cooling which has also been used very successfully for cell sonication.[31] However heat removal becomes increasingly difficult with increasing system volume. Designing efficient acoustics is essential to achieve a high ratio of pressure amplitude to heat. 10 years ago most acoustic chambers were designed as bonded multilayer structures operating in the compression mode to form a single span coherently resonating stack of the type shown in Fig. 7. Several one dimensional model approaches[6,40,51] were developed[17,25,39] for this structure, which were experimentally verified[6,50,54] as seen in Fig. 8. However over the past 10 years the design of most micro-fluidic acoustic systems has moved to applying the sound from one side. In these systems the mode carrying the vibrations into the fluid chamber is not a controlled compression wave. A multi-wavelength system which operates in a similar manner is shown in Fig. 3. In this case the piezoelectric element is pressed to one side of a glass duct. This approach has minimal heat transfer from the drive element to the duct and since all parts are relatively unconstrained interface losses are also minimised. The next section describes some of the requirements for developing this type of system.

4.2 Creating a standing wave: Selection of a particular wall mode is not always required

Compression waves entering a liquid from a solid experience very little attenuation over long distances. Travelling shear waves, in contrast, decay in water within 0.5 μm of the surface at 5 MHz.[89] A small propagation length (an evanescent wave) is also produced when the wavelength in the solid is less than in the liquid, as described in parts 3 and 21 of this tutorial series.[12,90] However when the water dimension is resonant there is very little difference between a wave produced by a compression or a shear device.[89] In both cases the vibration energy converts to a compression mode in the water. Based on the assumption that it does not matter which mode produces the vibrations, then the critical factor is delivering vibrations energy at the resonant frequency of the fluid-cavity. For an in-depth description of waveforms at fluid interfaces tutorial 17[91] is recommended.

There is also freedom to switch between mode types in the solid components. This is demonstrated by the example of the multimode system in Fig. 3 where a compression mode in the PZT converts to a flexural mode in the glass duct and then back to a compression mode in the liquid. The conversion between the two solids is achieved by maintaining minimal contact between them, ensuring that variation in mode shape between these parts does not cause interference (or transfer heat).

Minimal contact also allows each element to be separately modelled and optimised for maximum vibrations. Although mode-conversion is widely used with sub-wavelength systems only one other minimal contact particle manipulation system has been reported.[61] However the modelling approach is well established within the field of Non Destructive Testing applications and an outline description is given in the next section.[92–94] Since this minimal contact approach is at an early stage of development for particle manipulation, researchers choosing this method should proceed with some caution: Although minimal contact potentially allows high Q and therefore increased efficiency, the weak coupling can lead to complex ''beating'' variations in power levels between the components. Also systems requiring fast switching between modes (currently used to enhance separation in multi-wavelength systems,[82] and to control position in sub-wavelength systems) will have their speed limited by the ''ring down'' and rise as Q is increased (the relationship is given in section 2.1).

In air-based systems the loading and coupling back from the air to the structure can be ignored and so even the fluid (air) and its container can be modelled separately. This is not possible for liquids which will strongly affect the resonance frequency of the driving structure. Therefore although the PZT drive can be modelled separately a liquid and its chamber should always be modelled together.

4.3 Modelling resonant parts

The modelling path. 1. Choose the operating frequency: In water filled chambers this should be above 1 MHz to avoid cavitation effects, in air much lower frequencies can be used but forces increase with frequency.

2. Define the internal resonant dimensions: For a parallel wall chamber the distance between the walls must be a multiple of half wavelengths, $n\ c/2f$ where n is an integer. For tubular chambers (see Fig. 1B, 1D and 1F and 10) the diameter is $x_n c/\pi f$ where x_n is from the Bessel series 3.813, 7.015, 10.173 ($J_1(x) = 0$). When $n > 20$ the size is less critical since a 5% change in operating frequency is usually possible.

3. Match the wall mode shape to the fluid mode shape at the operating frequency. This is not usually carried out for MHz chambers with substantial walls because at these frequencies there are so many resonances that selection of one mode is difficult. In lower frequency air fill chambers matching mode shape of the fluid and the wall is used[95] while for higher frequencies this is under development.

4.4 Modelling the chamber wall

For simplicity a rectangular bar of aluminium is described here. The fundamental symmetric (compression) modes S0 occur when the length, l is an integer multiple of the half wavelength, the first two harmonics are shown in Fig. 21. These first harmonics can be accurately predicted by:

$$\lambda/2=\sqrt{(E/\rho(1-v^2))/2f} \qquad (12)$$

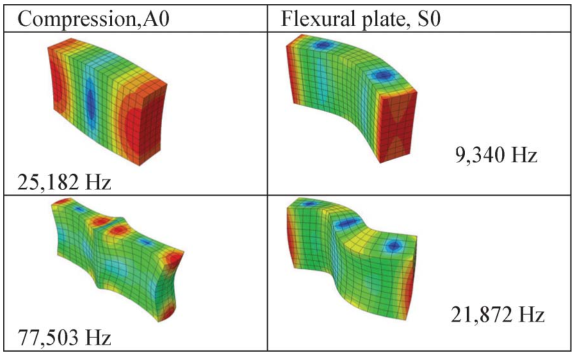

Fig. 21 Aluminium bar 100 × 50 × 20 mm showing displacement (not to scale) predicted by Abaqus.[96] First harmonics (upper line) and second harmonics (lower line) are shown for zero order anti-symmetric and symmetric waves in the length direction. Colours indicate displacement magnitude (3 dimensions combined), blue low, red high.

where E is the elastic (Young's) modulus (70.8 GPa), ρ is the density 2700 kgm^{-3}, v is Poisson's ratio (0.3375) and f is the frequency. The wavelength depends on the phase velocity not the bulk velocity. Phase velocity varies with frequency as shown in the dispersion plot Fig. 22 (obtained with the modelling program Disperse[97]) and therefore the higher harmonics are not predicted by eqn (12) (as indicated by the divergence of the red symbols in Fig. 22). There are analytical solutions for many other shapes, for these the tables compiled by Blevins[98] are recommended. Analytical solutions are also given for another mode the anti-symmetric (flexural plate) mode A0 which is also shown in Fig. 21. The analytical solution for the A0 mode is more difficult but the agreement with the disperse curves is good at all harmonics. Numerical solutions for the compression and the flexural plate modes for the 100 × 50 × 20 mm aluminium bar are also included in Fig. 22 (including those presented in Fig. 21). Agreement between numerical solutions and dispersion curves is very high and is calculated on the basis of $n0.5\lambda$ for resonances in the compression mode and $(n0.5 + 0.25)\ \lambda$ for the flexural wave mode.

It is convenient to use the three modelling methods together. In addition to the mode velocities, Disperse, and

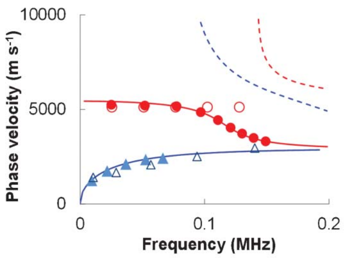

Fig. 22 Resonant modes in an aluminium bar 100 × 50 × 20 mm, red = compression S0, blue = flexural A0 correspond with Fig. 21. (dotted lines top right are higher modes). Lines are predicted by Disperse, Open symbols are numerical predictions, filled symbols are 3D models from Abaqus.[96]

other mode tracking methods, provide useful representation of the mode shape for single and multi-layered stacks and tubes, including fluid layers but with only one finite dimension. 3D stress analysis models from programs such as Comsol[99] and Abaqus[96] provide the most complete solutions (and require the most specialist knowledge), since current versions do not include mode tracking functions, a program such as Disperse is useful for most predictive design work. Identifying modes becomes more difficult as the number of wavelengths increases, stability of operation also becomes more difficult therefore as a rule the number of wavelengths in one dimension should not exceed 15.

Models of this type will allow chambers to be constructed where the wave shape in the wall matches the wave shape in the fluid. The aim is to increase efficiency and control streaming patterns.

The next step is to test the system and confirm that the wave-shapes have been created.

4.5 Experimental confirmation

The ideal method to confirm that model predictions of the acoustic fields are correct, is to test the chamber with a particle suspension and look at the particle distribution. This is not possible using small chambers that are either opaque or manifest acoustic streaming. However in large chambers there are several options which can be used:

1) A high frequency microphone is useful for confirming the sound output level; a nozzle placed on the front can help monitor small regions.

2) Sand, glass beads or liquid placed on the surface will identify the mode shape by forming Chladni figures,[100,101] see Fig. 23.

3) A scanning laser vibrometer (if available) provides non-invasive confirmation of all the mode shapes across frequency range.

Agreement between model and modes on the outside of a chamber gives confidence in the model predictions for the inside.

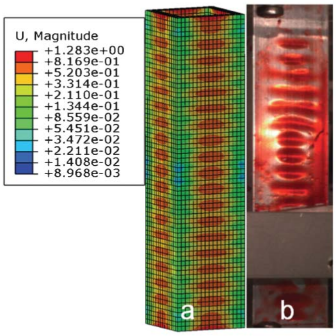

Fig. 23 Experimental confirmation of modelled mode shape predictions in an aluminium duct (20 × 20 × 100 mm OD) a) A stress analysis (Abaqus) model of the duct showing transverse velocity antinodes nodes at 206 kHz. b) Confirmation of the model with a liquid Chladni figure. Water with red food colouring moves to the same pattern of antinodes on the surface of the duct when driven at 203 kHz. (The horizontal bar across the lower section is holding the piezoelectric transducer in place).

Since it is possible to build a system without knowledge of the wave shape in the walls these considerations in section 4.4 and 4.5 are not usually taken into account. However as the need for efficiencies of power and particle positioning increase, the techniques described in this section are likely to become more important.

Definitions

Nomenclature

Cp	Specific heat capacity at constant pressure. 4180 (J kg^{-1} °C^{-1})
c_0	Speed of sound
c_y	Cell concentration, yeast ml^{-1}
g	Acceleration, due to gravity 9.8 (m s^{-2}).
d	Channel depth (m)
e	Base of the natural logarithm
E	Elastic modulus (Pa)
f	Frequency (Hz)
f_0	Resonant frequency (Hz)
Gr	Grashof number, $g\alpha(T_h - T_c)H^3/\upsilon^2$
h	Internal channel height (m)
k	Thermal conductivity 0.607 (W m^{-1} °C^{-1})
L_0	The length scale (m)
L_e	Entrance length (m)
Nu	Nusselt number (Convective heat transfer/ conductive heat transfer)
Pr	Prandtl number, ν/κ
Q'	Flow rate (m^{3}s^{-1})
Q'_{max}	Maximum non turbulent flow rate
Q_{eff}	Effective Q-factor of multiple parts $2\pi\varepsilon$/power loss
Q_{susp}	Q-factor of the suspension
r_c	Cell clump of radius $\lambda/8$ (m)
Ra	Rayleigh number, Gr Pr
Re	Reynolds number, $\rho_f\, \nu_{av} L_0/\eta$
T_c T_h	Temperature of walls (°C)
ν_{av}	Average velocity across tube (m s^{-1})
ν_f	Bulk fluid velocity (m s^{-1})
ν_c	Clump velocity (m s^{-1})
ν_z	Velocity at z from the channel centre (m s^{-1})
w	Internal chamber width (m)
x_n	Bessel series
z	Distance from centre of channel (m)

Greek letters

A	Acoustic absorption coefficient
α_v	Volume (or cubic) thermal expansion dynamic viscosity of the fluid 0.256 × 10^{-3}(kg m^{-1}s^{-1}).
ε	Stored energy (J)
κ	Thermal diffusivity, k/ρCp 1.45 × 10^{-7}(J^{2}C^{-2} m^{-4}s^{-1})
Λ	Wavelength of sound (m)
Λ	Mass density ratio particle fluid

P	Density (kg m^{-3})
ρ_c	Cell density- yeast 1.114×10^3 (kg m^{-3})
ρ_f	Fluid density 997 (kg m^{-3})
η	Dynamic viscosity of the fluid 9×10^{-4} (kg m^{-1} s^{-1} or Pa s)
Σ	Speed of sound ratio particle/fluid
Υ	Kinematic viscosity, η/ρ_f (m^2 s^{-1})

Values given are for water are at 25 °C[102] where not stated otherwise.

Acknowledgements

Our thanks to Dr Nicola J. Hawkes for editing assistance.

References

1 H. Bruus, *Lab Chip*, 2012, **12**, 1014–1021.
2 M. Wiklund, *Lab Chip*, 2012, **12**, 2018–2028.
3 G. G. Yaralioglu, I. O. Wygant, T. C. Marentis and B. T. Khuri-Yakub, *Anal. Chem.*, 2004, **76**, 3694–3698.
4 A. Lenshof, M. Evander, T. Laurell and J. Nilsson, *Lab Chip*, 2012, **12**, 684–695.
5 A. Lenshof, C. Magnusson and T. Laurell, *Lab Chip*, 2012, **12**, 1210–1223.
6 P. Glynne-Jones, R. J. Boltryk and M. Hill, *Lab Chip*, 2012, **12**, 1417–1426.
7 P. Augustsson and T. Laurell, *Lab Chip*, 2012, **12**, 1742–1752.
8 J. D. Adams, C. L. Ebbesen, R. Barnkob, A. H. J. Yang, H. T. Soh and H. Bruus, *J. Micromech. Microeng.*, 2012, **22**, 1–8.
9 A. Lenshof, A. Ahmad-Tajudin, K. J. Rås, A.-M. S. rd-Nilsson, L. Åberg, G. Marko-Varga, J. Malm, H. Lilja and T. Laurell, *Anal. Chem.*, 2009, **81**, 6030–6037.
10 H. Bruus, *Lab Chip*, 2011, **11**, 3742–3751.
11 H. Bruus, *Lab Chip*, 2012, **12**, 1578–1586.
12 J. Dual and T. Schwarz, *Lab Chip*, 2012, **12**, 244–252.
13 H. Bruus, *Lab Chip*, 2012, **12**, 20–28.
14 J. Dual and D. Möller, *Lab Chip*, 2012, **12**, 506–514.
15 J. Dual, P. Hahn, I. Leibacher, D. Möller and T. Schwarz, *Lab Chip*, 2012, **12**, 852–862.
16 S. S. Sadhal, *Lab Chip*, 2012, **12**, 2292–2300.
17 S. S. Sadhal, *Lab Chip*, 2012, **12**, 2600–2611.
18 M. Wiklund, R. Green and M. Ohlina, *Lab Chip*, 2012, **12**, 2438–2451.
19 S. Peterson, G. Perkins and C. Baker, in *IEEE 8th Annual Conference of the Engineering in Medicine and Biology Society*, 1986, pp. 154–156.
20 C. M. Cousins, P. Holownia, J. J. Hawkes, M. S. Limaye, C. P. Price, P. J. Keay and W. T. Coakley, *Ultrasound Med. Biol.*, 2000, **26**, 881–888.
21 G. Whitworth, M. A. Grundy and W. T. Coakley, *Ultrasonics*, 1991, **29**, 439–444.
22 L. Gherardini, C. Cousins, J. J. Hawkes, J. Spengler, S. Radel, H. Lawler, B. Devcic-Kuhar, M. Gröschl, W. T. Coakley and A. J. McLoughlin, *Ultrasound Med. Biol.*, 2005, **31**, 261–272.
23 S. Kogan, G. Kaduchak and D. N. Sinha, *J. Acoust. Soc. Am.*, 2004, **116**, 1967–1974.
24 E. Benes, F. Hager, W. Bolek and M. Gröschl, in *Ultrasonics International' 91*, Butterworth-Heinemann, Oxford, UK, 1992, pp. 167–170.
25 B. Lipkens, J. Dionne, A. Trask, B. Szczur, A. Stevens and E. Rietman, *Phys. Procedia*, 2010, **3**, 263–268.
26 Z. Wang, P. Grabenstetter, D. L. Feke and J. M. Belovich, *Biotechnol. Prog.*, 2004, **20**, 384–387.
27 M. J. Anderson, R. S. Budwig, K. S. Line and J. G. Frankel, *IEEE Ultrasonics Symposium*, 2002, 464–467.
28 E. Riera, J. A. Gallego-Juarez and T. J. Mason, *Ultrasonics Sonochemistry*, 2006, **13**, 107–116.
29 I. Gonzalez, T. L. Hoffmann and J. A. Gallego, *J. Aerosol Sci.*, 2000, **31**, 1461–1468.
30 T. J. Mason and J. P. Lorimer, *Applied Sonochemistry: Uses of Power Ultrasound in Chemistry and Processing*, John Wiley & Sons, Chichester, 2002.
31 K. A. J. Borthwick, W. T. Coakley, M. B. McDonnell, H. Nowotnyc, E. Benes and M. Gröschl, *J. Microbiol. Methods*, 2005, **60**, 207–216.
32 E. A. Brujan, T. Ikeda and Y. Matsumoto, *Exp. Therm. Fluid Sci.*, 2008, **32**, 1188–1191.
33 J. J. Hawkes and W. T. Coakley, *Enzyme Microb. Technol.*, 1996, **19**, 57–62.
34 M. Gröschl, *Acta Acust. Acust.*, 1998, **84**, 815–822.
35 M. Gröschl, *Acta Acust. Acust.*, 1998, **84**, 632–642.
36 J. J. Hawkes, M. S. Limaye and W. T. Coakley, *J. Applied Microbiology*, 1997, **82**, 39–47.
37 S. Radel, L. Gherardini, A. J. McLoughlin, O. Doblhoff-Dier and E. Benes, *Bioseparation*, 2000, **9**, 369–377.
38 S. Radel, *Elektrotech. Informationstech.*, 2009, **126**, 51–57.
39 H. Böhm, L. G. Briarty, K. C. Lowe, J. B. Power, E. Benes and M. R. Davey, *Biotechnol. Bioeng.*, 2003, **82**, 74–85.
40 M. Hill and R. J. K. Wood, *Ultrasonics*, 2000, **38**, 662–665.
41 E. Benes, M. Gröschl, H. Nowotny, F. Trampler, T. Keijzer, H. Böhm, S. Radel, L. Gherardini, J. J. Hawkes, R. König and C. Delouvroy, in *IEEE Ultrasonics Symposium*, Atlanta, 2001, pp. 649–659.
42 S. Radel, in *Institut für Allgemeine Physik*, TU Wien, Vienna, 2003.
43 S. Gupta and D. L. Feke, *AIChE J.*, 1998, **44**, 1005–1014.
44 M. Gröschl, *Acta Acust. Acust.*, 1998, **84**, 432–447.
45 R. Nawrodt, A. Zimmer, T. Koettig, C. Schwarz, D. Heinert, M. Hudl R. Neubert, Matthias Thürk, S. Nietzsche, W. Vodel, P. Seidel and A. Tunnermann, in *7th Edoardo Amaldi Conference on Gravitational Waves (Amald7)*, IOP, 2008.
46 T. M. P. Keijzer, F. Trampler, A. Oudshoorn, O. Doblhoff-Dier and H. v. d. Berg, in *Cell Culture Engineering, VII*, Snowmass Village, Colorado, USA, 2002.
47 R. Barnkob, P. Augustsson, T. Laurell and H. Bruus, *Lab Chip*, 2010, **10**, 563–570.
48 P. Augustsson, R. Barnkob, S. T. Wereley and H. Bruus, *Lab Chip*, 2011, **11**, 4152–4164.
49 M. Hill, Y. Shen and J. J. Hawkes, *Ultrasonics*, 2002, **40**, 385–392.
50 M. Hill, R. J. Townsend and N. R. Harris, *Ultrasonics*, 2008, **48**, 521–528.
51 H. Nowotny and E. Benes, *J. Acoust. Soc. Am.*, 1987, **82**, 513–521.

52 M. Schmid, E. Benes and R. Sedlaczek, *Meas. Sci. Technol.*, 1990, **1**, 970–975.

53 R. Schnitzer, C. Reiter, K.-C. Harms, E. Benes and M. Gröschl, *IEEE Sens. J.*, 2006, **6**, 1314–1322.

54 J. J. Hawkes, W. T. Coakley, M. Gröschl, E. Benes, S. Armstrong, P. J. Tasker and H. Nowotny, *J. Acoust. Soc. Am.*, 2002, **111**, 1259–1266.

55 E. Benes, M. Gröschl, F. Seifert and A. Pohl, *IEEE Trans. Ultrason. Ferroelectr. Freq. Control*, 1997, **45**, 1314–1330.

56 L. Gherardini, S. Radel, S. Sielemann, O. Doblhoff-Dier, M. Gröschl, E. Benes and A. J. McLoughlin, *Bioseparation*, 2001, **10**, 153–162.

57 M. A. Sobanski, C. R. Tucker, N. E. Thomas and W. T. Coakley, *Bioseparation*, 2001, **9**, 351–357.

58 S. Radel, A. McLoughlin, L. Gherardini, O. Doblhoff-Dier and E. Benes, *Ultrasonics*, 2000, **38**, 633–637.

59 C. S. Kwiatkowski and P. L. Marston, *J. Acoust. Soc. Am.*, 1998, **103**, 3290–3300.

60 M. Greenspan and C. E. Tschiegg, *J. Acoust. Soc. Am.*, 1959, **31**, 75–76.

61 G. Goddard and G. Kaduchak, *J. Acoust. Soc. Am.*, 2005, **117**, 3440–3447.

62 E. Benes and F. Hager, *Br. pat.,* PCT/AT1989/000098, Austria, 1990.

63 P. Glynne-Jones, R. J. Boltryk, N. R. Harris, P. Baclet and M. Hill, *JASA Express Lettters*, 2009, **126**, EL75–EL79.

64 F. Trampler, in *Institut für Allgemeine Physik*, TU Wien, Vienna, 2000.

65 K. Yosioka and Y. Kawasima, *Acustica*, 1955, **5**, 167–172.

66 H. Bruus, *Theoretical Microfluidics*, Oxford University Press, Oxford, 2008.

67 J. J. Hawkes and W. Terence, *Sens. Actuators, B*, 2001, **75**, 213–222.

68 J. J. Hawkes, D. Barrow, J. Cefai and W. T. Coakley, *Ultrasonics*, 1998, **36**, 901–903.

69 J. F. Douglas, J. M. Gsiorek, J. A. Swaffield and L. B. Jack, *Fluid Mechanics*, Prentice Hall, Harlow, England; New York, 2011.

70 F. M. White, *Viscous Fluid Flow*, McGraw-Hill, New York, 1991.

71 F. Trampler, S. A. Sonderhoff, P. W. S. Pui, D. G. Kilburn and J. M. Piret, *Biotechnology*, 1994, **12**, 218–284.

72 N. Seki, S. Fukusako and H. Inaba, *J. Fluid Mech.*, 1978, **84**, 695–704.

73 D. J. Tritton, *Physical Fluid Dynamics*, Clarendon Press, Oxford, 1988.

74 M. Wiklund, *Lab Chip*, 2012, **12**, 2018–2028.

75 N. Seki, S. Fukusako and H. Inaba, *Wärme- und Stoffübertragung*, 1978, **11**, 145–156.

76 M. A. Grundy, in *Pure and Aplied Biology*, University of Wales Cardiff, Cardiff, 1994.

77 J. J. Hawkes, J. J. Cefai, D. A. Barrow, W. T. Coakley and L. G. Briarty, *J. Phys. D: Appl. Phys.*, 1998, **31**, 1673–1680.

78 B. Atkinson, M. P. Brocklebank, C. C. H. Card and J. M. Smith, *AIChE J.*, 1969, **15**, 548–553.

79 R. Y. Chen, *Trans. ASME, J. Fluids Engineering.*, 1973, **95**, 153–158.

80 N. Dombrowski, E. A. Foumeny, S. Ookawara and A. Riza, *Can. J. Chem. Eng.*, 1993, **71**, 472–476.

81 M. Friedmann, J. Gillis and N. Liron, *Appl. Sci. Res.*, 1968, **19**, 426–438.

82 Y. Liu and K.-M. Lim, *Lab Chip*, 2011, **11**, 3167–3173.

83 J. J. Hawkes, R. W. Barber, D. R. Emerson and W. T. Coakley, *Lab Chip*, 2004, **4**, 446–452.

84 L. Castillo, X. Wang and W. K. George, *J. Fluids Eng.*, 2004, **126**, 297–304.

85 E. M. Sparrow, J. P. Abraham and W. J. Minkowy, *Int. J. Heat Mass Transfer*, 2009, **52**, 3079–3083.

86 A. H. Gibson, *Philos. Trans. R. Soc. London*, 1910, **83**, 366–378.

87 D. L. Cochran and S. J. Kline, in *National Advisory Committee for Aeronautics*, Stanford University, 1958.

88 K. Uchino, *Smart Mater. Struct.*, 1998, **7**, 273–285.

89 T. W. Schneider and S. J. Martin, *Anal. Chem.*, 1995, **67**, 3324–3335.

90 M. Wiklund, S. Radel and J. J. Hawkes, *Lab Chip*, 2012, 12.

91 M. Gedge and M. Hill, *Lab Chip*, 2012, **12**, 2998–3007.

92 M. J. S. Lowe and P. Crawley, *J. Nondestr. Eval.*, 1994, **13**, 185–200.

93 M. Castaings and M. J. S. Lowe, *J. Acoust. Soc. Am.*, 2008, **123**, 696–708.

94 W. J. Jacobi, *J. Acoust. Soc. Am.*, 1949, **21**, 120127.

95 G. Kaduchak, D. N. Sinha and D. C. Lizon, *Rev. Sci. Instrum.*, 2002, **73**, 1332–1336.

96 S. Abaqus, *Unified FEA Software*, Dassault Systemes.

97 B. Pavlakovic and M. Lowe, *Disperse, Software for generating dispersion curves, Mechanical Engineering*, Imperial College, London, 2011, **2.0.16i**.

98 R. D. Blevins, *Formulas for Natural frequency and mode shape*, Krieger Publishing Company Malbar, Florida 2001.

99 M. M. Comsol, *Finite Element Analysis, and Engineering Simulation Software*.

100 E. F. F. Chladni, *Entdeckungen über die Theorie des Klanges, Discoveries Concerning the Theory of Music*, Weidmanns Erben und Reich, Leipzig, 1787.

101 M. Faraday, *Philos. Trans. R. Soc. London*, 1831, **121**, 299–340.

102 *CRC Handbook of Chemistry and Physics*, CRC Press, 2002–2003.